PAPER

Defect structure–performance correlation in Eu³⁺@UiO-66: design of coordination sites for rapid optical O_2 sensing

Zhenyu Zhao [ID] and Michael Tiemann [ID] *

Defect engineering offers an effective route to tailor the local coordination environment, gas transport and excited-state processes in metal–organic frameworks (MOFs). We establish a quantitative structure–property relationship linking defect-modulated porosity in UiO-66-based MOFs to the Stern–Volmer parameter for O_2 sensitivity. By systematically introducing three distinct defect types, we reveal that vacancy formation increases the accessibility of Eu^{3+} sites and accelerates O_2 diffusion, thereby enhancing dynamic quenching, while simultaneously introducing a non-negligible static contribution. An optimal defect concentration (represented by S_{BET}) is identified for highest O_2 gas response, arising from a balance between O_2 accesibility and the availability of active quenching sites. Phase-correlated luminescence decay measurements show a clear reduction of Eu^{3+} lifetime upon switching from N_2 to ambient air, confirming the contribution of the collisional quenching pathway. The resulting nonlinear Stern–Volmer behaviour is rationalized by an apparent quenching constant $K_{app,SV}$, incorporating both the intrinsic quenching rate, the native lifetime, and a structural factor H that reflects defect-dependent porosity. A volcano-type dependence of sensing efficiency on defect concentration further highlights the competing roles of Eu^{3+} exposure and diffusion resistance. This study provides a mechanistic framework for defect-regulated triplet quenching in porous solids and offers a general design principle for lanthanide-based porous optical oxygen sensors. The general design principle established in this study is that defect-engineered, O_2-accessible coordination environments can be used to balance mass transport and triplet-state energy transfer, thereby maximizing lanthanide-based O_2 sensing performance.

Introduction

The detection and quantification of molecular oxygen are crucial for a wide range of scientific and industrial applications, including environmental monitoring, corrosion science, catalysis, and aerospace engineering. Among the available strategies, luminescence-based O_2 sensors are particularly attractive because they enable non-invasive, rapid, and highly sensitive detection of O_2 through optical read-out. An ideal optical O_2 sensor should therefore exhibit a stable, reversible, and quantitative luminescent response to variations in O_2 concentration.[1]

To meet these requirements, a wide range of luminescence-based O_2-sensing systems have been developed, including lanthanide complexes and organic dyes immobilized in solid matrices, including polymers, silica, or zeolites.[2] In recent years, luminescent metal–organic frameworks (MOFs) have emerged as a versatile class of materials for optical O_2 sensing owing to their well-defined crystalline structures, tunable porosity, and chemically uniform microenvironments for hosting or coordinating luminophores. The photoluminescence of MOFs can originate from multiple emissive centers – organic linkers, metal nodes, or encapsulated guest molecules – and energy transfer processes among these components have been extensively exploited to tailor their optical performance.[3,4]

Within this context, MOFs can operate in two main modes for O_2 detection: (1) as porous matrices encapsulating O_2-sensitive emitters,[5–8] or (2) as intrinsically emissive frameworks, in which excited states localized on linker or metal sites are dynamically quenched by triplet molecular oxygen.[9–12] Within the broad family of metal–organic frameworks (MOFs), zirconium-based systems have attracted particular attention owing to their versatile topologies and high thermal and chemical stability.[13–15] Among them, UiO-66 and its isoreticular derivatives, first reported by Cavka et al., have been extensively investigated over the past decade as prototypical Zr-MOFs.[16] As with many crystalline porous materials, UiO-type frameworks can host a variety of structural defects, and the study of such defective phases has become a research hotspot.[17] Under controlled reaction conditions, including temperature, synthesis duration, and the type or

Paderborn University, Department of Chemistry, Warburger Str. 100, 33098 Paderborn, Germany. E-mail: michael.tiemann@upb.de

amount of modulators, the defect concentration can be tuned.[18] The defect-engineering strategy enables the deliberate introduction of terminal species, typically carboxylic acids, that coordinate to Zr^{4+} in the $[Zr_6O_4(OH)_4]^{12+}$ nodes ('Zr_6 clusters') and thereby create open or chemically modified metal sites. Several approaches for generating non-coordinating (dangling) carboxylate groups have been reported by DeCoste et al.,[19] Oozeerally et al.,[20] and Song et al.[21] Recent studies have further revealed that these defect-modulated UiO-frameworks exhibit enhanced optical and sensing properties upon incorporation of lanthanide ions.[22,23]

In this study, we present a defect-assisted strategy to construct robust Eu^{3+} coordination sites within UiO-66 frameworks by incorporating different auxiliary dicarboxylic acids. The resulting Eu-functionalized UiO-66 materials display efficient and reversible luminescent responses toward molecular oxygen, enabling the detection of O_2 concentrations as low as 1500 ppm. These materials thus hold strong potential for low-concentration O_2 sensing applications under ambient conditions. Time-resolved photoluminescence measurements reveal a pronounced lifetime shortening in the presence of O_2, confirming a part of dynamic quenching process between the excited Eu^{3+} centers and triplet O_2 molecules. Another valuable result is that, although gas diffusion cannot be directly quantified in most porous systems, its influence can be inferred through structural descriptors such as porosity. By correlating BET surface areas with the Stern–Volmer coefficients, we uncover a distinct volcano-type structure-performance relationship, indicating that the O_2-sensing efficiency is maximized at intermediate defect concentrations. In this regime, site accessibility to O_2 and effective diffusivity are simultaneously optimized, whereas excessively low or excessively high defect densities in our defect-engineering groups of materials suppress the quenching-based response.

Experimental section

Chemicals

Zirconium chloride ($ZrCl_4$, 99.5%, Thermo Fisher Scientific, Germany), terephthalic acid (H_2BDC, 98%, Thermo Fisher Scientific, Germany), oxalic acid (H_2ox, 98%, Sigma-Aldrich, Germany), fumaric acid (H_2fum, 98%, BLD pharm), isophthalic acid (H_2ipa, 98%, BLD pharm), europium nitrate hexahydrate ($Eu(NO_3)\cdot 6H_2O$, 99.9%, Thermo Fisher Scientific, Germany), N,N'-dimethylformamide, isopropanol, methanol and ethanol ($\geq$ 99%, Sigma-Aldrich, Germany) were used as received.

Synthesis

The synthesis protocol for UiO-66 was adapted from the method reported by Katz et al., with modifications to the metal-to-linker ratio, solvent volume, and hydrochloric acid concentration to achieve the desired defect levels.[24] To further improve the crystallinity of the resulting materials, the solvothermal temperature and reaction duration were optimized relative to the original protocol.

Pristine network. $ZrCl_4$ (514.97 μmol, 1 equiv.) and terephthalic acid (669.35 μmol, 1.3 equiv.) were dispersed in 15 mL of N,N'-dimethylformamide (DMF) and sonicated for 15 min to obtain a homogeneous suspension. Subsequently, 1 mL of concentrated hydrochloric acid was added, and the mixture was further sonicated for another 15 min until a clear solution was obtained. The solvothermal reaction was carried out in a sealed glass vial placed in a programmable convection oven (Thermo Scientific Heraeus, U-series, Germany) at 120 °C for 48 h. After cooling to room temperature, the resulting white solid was collected by centrifugation and washed three times with DMF, isopropanol and ethanol. The product was dried at 60 °C for 12 h and is referred to as "UiO-66-*as*" (as-synthesized).

One-pot synthesis of defective UiO-66 based on oxalic acid (UiO-66–*x*-ox) and fumaric acid (UiO-66–*x*-fum). Defective UiO-66 materials were synthesized by a one-pot solvothermal procedure analogous to that of the pristine UiO-66 network, except for the addition of a defined amount of aliphatic dicarboxylic acid as a modulator. Specifically, oxalic acid (H_2ox) or fumaric acid (H_2fum) was introduced in varying molar equivalents (x) relative to the metal precursor ($ZrCl_4$). These two linear dicarboxylic acids can competitively coordinate to Zr_6-clusters during framework assembly, partially replacing the original BDC linkers and thereby generating missing-linker-type defects. The detailed quantities of all reagents used for each synthesis are summarized in Table S1 (SI). The obtained compounds are denoted as UiO-66-*x* ox and UiO-66-*x* fum, where *x* represents the molar equivalent of the aliphatic acid to the zirconium source. It needs to be stressed that *x* does not represent the absolute defect concentration but provides a relative and internally consistent metric for comparing samples within the same series of syntheses.

Mixed linker synthesis of UiO-66 using isophthalic acid (ipa). A mixed-linker strategy was employed to incorporate isophthalic acid (H_2ipa) as a secondary linker together with terephthalic acid (H_2BDC). The synthesis procedure of UiO-66-*x*-ipa followed that of the pristine UiO-66 network, with the linker composition adjusted according to the desired mixing ratio. In contrast to BDC, isophthalic acid is a bent dicarboxylate ligand that cannot bridge Zr_6-clusters. As a result, its incorporation disrupts long-range framework connectivity and induces a distinct defect environment compared to linear dicarboxylate modulators. Detailed reagent quantities and linker ratios are provided in Table S1 (SI). The resulting materials are denoted as UiO-66-*x*-ipa, where *x* represents the relative molar fraction of isophthalic acid in the total linker mixture.

Activation

All UiO-66 based samples were activated in two consecutive steps. In the first step, a methanol solvent–exchange procedure was performed twice under static conditions to remove residual N,N'-dimethylformamide (DMF) from the pore system.[25,26] Recent computational studies by Caratelli et al. have shown that the linkers in defective UiO-66 frameworks can undergo local dynamic motion or partial de-coordination in the presence of protic solvents such as methanol; nevertheless, the overall framework connectivity remains preserved.[27,28] In the second

step, the methanol-exchanged samples were thermally activated at 100 °C for 24 h to remove methanol from the pores. Prior to post-synthetic europium incorporation and physisorption measurements, the materials were further degassed at 150 °C for 12 h under dynamic vacuum to ensure complete solvent removal.

Post-synthetic incorporation of Eu

The activated UiO-66 materials synthesized in sections (a–c) (UiO-66-x ox, UiO-66-x fum and UiO-66-x ipa) were used for post-synthetic Eu(III) incorporation. In a typical procedure, the defective UiO-66 sample (60 mg, corresponding to one molar equivalent of the idea UiO-66 formula unit, $C_{48}H_{28}O_{32}Zr_6$) was dispersed in 4 mL of N,N'-dimethylformamide (DMF) containing Eu(NO$_3$)·6H$_2$O (20.91 mg, 1.3 equiv.) and sonicated to obtain homogeneous suspension. The mixture was then heated in a programmable convection oven at 100 °C for 12 h. The resulting white solid was collected by centrifugation and washed three times with DMF, isopropanol, and ethanol. The washed materials were subsequently subjected to the same solvent–exchange and activation procedures as described for the pristine frameworks. The obtained compounds are denoted as UiO-66-x ox-Eu, UiO-66-x fum-Eu and UiO-66-x ipa-Eu, where x retains the same definition as in the corresponding precursor series.

Structural characterization

Powder X-ray diffraction (PXRD) of all synthesized materials was performed on a Bruker D8 Advance diffractometer with Cu-Kα radiation (λ = 1.541 Å) and a step size of 2θ = 0.02°. Samples were mounted on PMMA holders, and reference PXRD patterns were simulated from CIF files (CCDC 733458) using the VESTA software.[29] Proton Nuclear Magnetic Resonance Spectroscopy (^{1}H-NMR) was employed to estimate the incorporated amounts of fumaric acid and isophthalic acid. Spectra were acquired on a Bruker Ascend 700 spectrometer. For sample digestion, 20 mg of the activated UiO samples were dispersed in 0.5 mL of saturated K$_3$PO$_4$/D$_2$O solution and sonicated for 10 min. After cooling, 0.2 mL of 1 M DCl/D$_2$O was added for acidification, resulting in immediate dissolution. N$_2$ physisorption isotherms were collected at 77 K using a Quantachrome Autosorb 6B analyzer over a relative pressure range of p/p_0 of 0–1. BET surface areas were determined according to the Rouquerol criteria, and total pore volume at p/p_0 = 0.89.[30] Pore size distributions were derived from the adsorption branch using the NLDFT model (silica kernel). TGA-MS (thermogravimetric analysis coupled with mass spectroscopy) was measured on a Linseis TG-P1000 thermobalance coupled with a Pfeiffer Vacuum GSD 301 O3 mass spectrometer. Samples were measured under Ar in the range of 30–800 °C with a heating rate of 10 °C min^{-1}. Scanning electron microscopy (SEM) and energy-dispersive X-ray spectroscopy (EDX) were conducted using a Zeiss NEON 40 microscope. Prior to measurement, the samples were sputter-coated with a thin gold layer to improve conductivity and mounted on conductive carbon pads. Attenuated total reflectance infrared (ATR-IR) spectra were obtained using a Bruker Vertex 70 spectrometer equipped with an ATR module at a resolution of 2 cm^{-1} and 64 Scans under ambient conditions. Raman spectra were recorded on the same instrument equipped with the RAM II module.

Luminescence studies

Steady-state and time-resolved luminescence measurements were performed on a Jasco FP-8300 spectrofluorometer equipped with a photomultiplier tube operated at 600 V. Three-dimensional excitation–emission spectra and two-dimensional emission spectra were collected with excitation and emission slit widths of 2.5 nm, unless stated otherwise. For the investigation of the O$_2$-sensing response, time-resolved luminescence experiments were carried out on the same instrument. The temporal evolution of the Eu^{3+} emission intensity at 614 nm was monitored upon excitation at 300 nm over 780 s under six different O$_2$ concentrations. From those measurements, the response/recovery time, Stern–Vomer relationship, and sample reproducibility were assessed. Luminescence lifetimes were measured using the phosphorescence lifetime mode of the JASCO FP-8300 with a chopping period of 25 s. Each measurement was based on the accumulation of 2500 data points to ensure reliable lifetime fitting.

O$_2$ gas sensing

For the preparation of UiO-66-based gas-sensing films, 15 mg of the activated sample was ground and dispersed in 1 mL of methanol, followed by sonication for 15 min. Approximately 1 μL of the resulting suspension was drop-cast onto a soda-lime glass substrate and heated at 75 °C on a hot plate (IKA RCT Basic, Germany) until completely dry. Soda-lime glass was selected owing to its low UV absorption and lack of background emission in the spectral range relevant to Eu-based MOFs.[31] The deposited layer was adjusted to be sufficiently thick to appear optically opaque when viewed from above. Prior to gas-response measurements, the prepared sensor was degassed under dynamic vacuum at 90 °C for 1 h to remove residual methanol from the pore voids. The O$_2$-sensing measurements were conducted in a custom-built gas cell (Fig. 1). Dry synthetic air (79.6% N$_2$ and 20.4% O$_2$, Air Liquide) was used as the test gas, while high-purity N$_2$ (99% N$_2$, Wöhning Gas) served as the carrier gas and purge gas. Gas mixtures with defined O$_2$ concentrations were introduced into the cell using mass flow controllers, maintaining a constant total flow rate of 300 mL min^{-1}.

Results and discussion

Material characterization

Isoreticular UiO-66-x ox, UiO-66-x fum and UiO-66-x ipa were synthesized and characterized. The selected ranges of x were determined by a combination of synthetic feasibility, phase stability and reproducibility considerations. The crystallinity of the solvothermally synthesized isoreticular UiO-66-based series of MOF materials was evaluated by powder X-ray diffraction (PXRD). Upon the gradual introduction of aliphatic dicarboxylic acids as modulators, no amorphization was observed, and all diffraction patterns remained consistent with that of the reference cubic UiO-66 phase (space group $Fm\bar{3}m$) (Fig. S1).[16] However, the
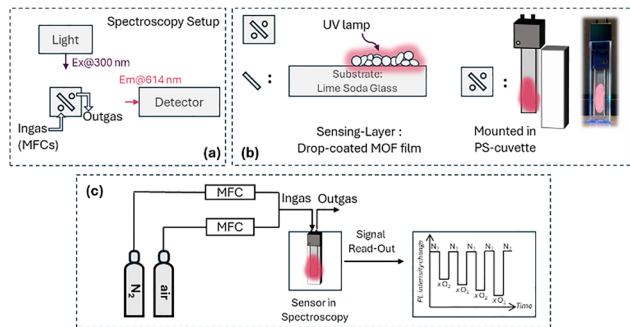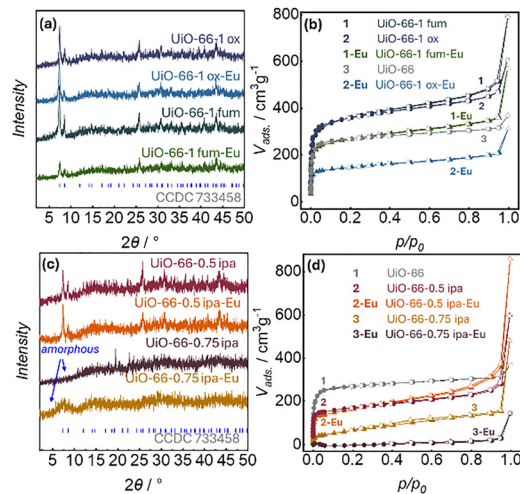
Fig. 1 Schematic illustration of the optical setup and gas-flow system used for O_2 sensing. (a) Excitation–emission geometry for monitoring Eu^{3+} emission from UiO–Eu films drop-cast on soda-lime glass (λ_{ex} = 300 nm; λ_{em} = 614 nm). (b) Custom-built gas cell containing the drop-cast MOF film on a glass substrate. (c) Complete gas-mixing and sensing setup: N_2 and synthetic air (20.5 vol% O_2) were combined using mass-flow controllers (MFCs) at a constant total flow rate of 300 mL min^{-1} for O_2-response measurements.

Fig. 2 Powder X-ray diffractograms and N_2 adsorption–desorption isotherms of defect-engineered UiO-66 frameworks before and after Eu^{3+} metalation. (a) and (b) Frameworks synthesized with oxalic and fumaric acids retain the fcu-topology and crystallinity upon Eu^{3+} incorporation, while a moderate reduction in surface area indicates partial occupation of defect sites. (c) and (d) In contrast, partial replacement of BDC by isophthalic acid (over 75%) leads to amorphization and severe loss of porosity, which is further maintained in their Eu^{3+}-metalated analogues. These results confirm that the coordination accessibility of defect sites is strongly dependent on the defect type and structural integrity of the UiO-network.

progressive decrease in peak intensities with increasing modulator content indicates reduced long-range order. Importantly, no additional diffuse or forbidden reflections appeared in the low-angle region (2θ = 2°–8°), confirming the absence of **reo**-type phase formation.[32] These results suggest that oxalic acid and fumaric acid likely coordinate to Zr^{4+} in the $[Zr_6O_4(OH)_4]^{12+}$ nodes ('Zr_6 clusters'), consistent with the defect engineering concept, in which auxiliary carboxylates partially replace terephthalate linkers or cap missing-linker sites.[33] Similar pre-coordination or substitution effects have been reported for other modulators, including fluoride-containing species[34] and even biomolecules.[35,36]

For mixed-isophthalate systems, crystalline but less-ordered products were obtained even when as much as 50% of terephthalate was replaced by isophthalate. This trend agrees with the findings of Song *et al.*[21] and Oozeerally *et al.*[20] who reported that the maximum incorporation of isophthalate into UiO-66 type networks is approximately 40%. Unlike terephthalate, isophthalate is a bent ligand and cannot simultaneously bridge two Zr_6-cluster in the required linear fashion. With increasing of isophthalate content, the geometric mismatch progressively disrupts long-range framework connectivity and as the result, for higher isophthalate fractions (75%), the PXRD patterns reveal a strong decrease in crystallinity relative to other samples in the same ipa-series (Fig. 2), suggesting the formation of an amorphous coordination polymer or a physical mixture of H_2BDC and H_2ipa under these conditions. A nearly perfect overlap between the PXRD patterns of the pristine UiO-series frameworks and their Eu^{3+}-incorporated derivatives confirms that both parent and Eu-loaded networks remain structurally intact.

Although PXRD results confirm phase retention, it does not allow determination of the precise Eu^{3+} incorporation mode. In principle, Eu^{3+} ions are expected to be coordinated by accessible terminal or pendant carboxylate sites, consistent with the strong affinity between Eu^{3+} and oxalate species well-known from lanthanide-oxalate separation chemistry.[37] The existence of lanthanide-fumarate[38] and lanthanide-isophthalate[39] coordination polymers further supports the plausibility of Eu-

carboxylate complexation within the defect-modified frameworks. In addition to coordination at defect or auxiliary linker sites, partial post-metalation at the Zr_6-clusters cannot be excluded. This possibility is consistent with previous reports on Ti^{4+} post-exchange in the UiO-66 framework[40] and the formation of UiO-type ***fcu***-frameworks constructed directly from lanthanide-based clusters.[41] Taken together, the data indicate that Eu^{3+} ions are incorporated in a manner that preserves the UiO-66 framework topology while occupying defect-associated or auxiliary ligand-derived coordination environments.

Thermogravimetric analysis coupled with mass spectrometry (TGA-MS) provides clear evidence that oxalic acid is incorporated in the UiO-66 structure as a defect-generating reagent. Compared to pristine UiO-66, both UiO-66-0.25-ox and UiO-66-1-ox exhibit an additional mass-loss step in the 200–350 °C region, which is absent in the defect-free material (Fig. S5). This intermediate decomposition feature has been widely reported as a characteristic marker of modulator-induced linker vacancies, where weakly bound monodentate species (*e.g.*, oxalate-derived fragments, formate-type residues, or partially substituted linkers) desorb or decompose at significantly lower temperatures than the terephthalate backbone.[20,42] The MS traces further confirm the defective nature of these species: pronounced m/z = 44 signals (CO_2^+) appear specifically in the intermediate temperature region, indicating thermolysis of small carboxylate-containing fragments. The intensity of this signal increases systematically from UiO-66-0.25-ox to UiO-66-1-ox, correlating with the amount of oxalic acid introduced during synthesis. In contrast, the major framework decomposition occurs at 450–550 °C, where both samples show

the expected collapse of the networks. However, UiO-66-1-ox displays a broadened and multi-step decomposition profile, consistent with a higher density of linker-vacancy defects and reduced structural stability. Collectively, the presence of the additional mass-loss step, the defect-specific CO_2 MS signal, and the broadened framework decomposition profile provide compelling evidence for the successful incorporation of oxalic acid-induced defects.

Unlike oxalate-based defective UiO-66 frameworks, detection of active protons on fumarate and isophthalate is possible with ^{1}H-NMR. Therefore, we quantified the linker compositions by solution ^{1}H-NMR after complete digestion of the MOF in phosphate buffer, followed by HCl-acidification to release the free organic acids while forming soluble Zr-phosphate clusters. This procedure ensures quantitative recovery of all linker species.[43,44] The relative amounts of BDC^{2-} (terephthalate) and the auxiliary dicarboxylates, determined from characteristic proton integrals, are summarized in Fig. S3 and Tabel S1. For the UiO-66-x-fum series, the fumarate content remains markedly lower than that of isophthalate in UiO-66-x-ipa. This limited incorporation likely arises from the strong competition between fumarate and terephthalate for coordination to the Zr_6 clusters and from the sensitivity of Zr-fumarate formation to acid modulators (e.g., formic acid generated from DMF decomposition).[45] Under mildly acidic solvothermal conditions, fumaric acid remains partially protonated, reducing its ability to participate in framework construction. Meanwhile, the dynamic coordination behavior intrinsic to UiO-type nodes allows the ligands to dissociate and re-attach during post-synthetic processing, enabling partial exchange of initially coordinated modulator fragments or even BDC itself.[46–48] After Eu^{3+} metalation, the ^{1}H NMR spectra show asymmetric splitting of the BDC resonances, reflecting the emergence of multiple coordination environments. Notably, the fumarate content decreases by ca. 50%, indicating dynamic dissociation of weekly bound fumarate during Eu^{3+} coordination. In contrast, the isophthalate fraction remains nearly unchanged, confirming the higher stability of the aromatic auxiliary linker (Fig. S3 and S4).

As shown in Fig. 3, UiO-66-x-ox, UiO-66-x-fum, and UiO-66-x-ipa exhibit sigmoidal type-I N_2 isotherms without hysteresis, confirming their microporous character. Since oxalic acid and fumaric acid molecules are shorter than H_2BDC, their incorporation reduces lattice connectivity and modulates the pore geometry. For UiO-66-ox and UiO-66-fum, the pore volume and BET surface area increase systematically with increasing aliphatic acid content, consistent with enlarged cavities and the defect-engineering trends reported by DeCoste et al.[19] The increase is more pronounced for oxalic acid, reflecting its stronger tendency to generate missing-linker defects. UiO-66-1-ox and UiO-66-0.75-ox reach exceptionally high BET surface areas (>1700 m^2 g^{-1}), exceeding theoretical predictions for defective UiO-66 with eightfold connectivity.[49] In contrast, incorporation of isophthalic acid progressively reduces both surface area and pore volume due to steric crowding by its bent aromatic geometry. Although comparable in length to BDC, isophthalate cannot function as a linear bridging linker and instead forms pendant groups that occupy
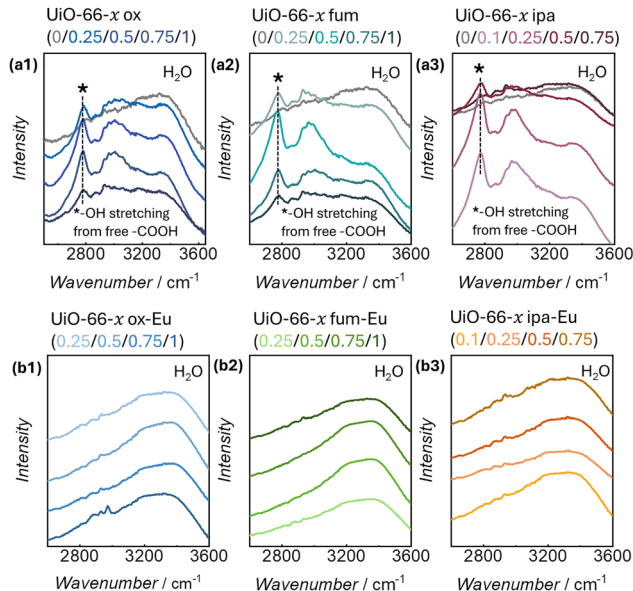

Fig. 3 FTIR evidence for Eu^{3+} coordination at defect-generating carboxylic acid sites. (a) FTIR spectra of UiO-66 and its oxalic, fumaric, and isophthalic-acids modified derivates display a distinct band at approximately 2800 cm^{-1}, corresponding to the O–H stretching vibration of uncoordinated –COOH groups. The intensity of this band increases systematically with defect-ligand content, confirming the generation of free carboxylic acid functionalities associated with linker-vacancy defects. (b) After Eu^{3+} coordination, this band disappears in all UiO-66-x-ox/fum/ipa samples, indicating that Eu^{3+} ions coordinate to these accessible carboxylate sites.

pore space. At high loadings (UiO-66-0.75-ipa), porosity has completely disappeared, consistent with PXRD evidence for amorphization and with the NLDFT pore-size analysis (Fig. S7, S9 and S11). Eu^{3+} incorporation causes a moderate reduction in N_2 uptake for all samples, attributable to partial pore occupation; however, the magnitude of the decrease is similar across all linker systems.

FTIR-ATR and Raman spectroscopy provide complementary insight into the coordination environment and ligand incorporation in the UiO-66 derivatives by probing their characteristic vibrational signatures.[50] Following the analytical approach proposed by Valenzano et al.,[51] several diagnostic regions were examined (enlarged views in Fig. S13, S15 and S17; full-range spectra in Fig. S12, S14 and S16). In the region of 500–600 cm^{-1}, the Zr–O–C stretching vibrations, a sensitive indicator of the Zr_6 cluster coordination sphere, undergoes a distinct shift upon incorporation of oxalic, fumaric or isophthalic acid. The shift reflects the altered bonding environment and cooperative interactions between the defect-generating ligands and the Zr_6 clusters. For the highly loaded UiO-66-0.75-ipa sample, which is identified as amorphous and nonporous by PXRD and N_2 sorption, the Zr–O band becomes significantly weaker and shifts to lower wavenumbers, indicating the formation of a Zr-carboxylate motif distinct from that in the ordered UiO-66 lattice. Additional characteristic features of the foreign dicarboxylates appear near 650 cm^{-1} (O–C–O bending) and 2790 cm^{-1} (O–H stretching of –COOH groups). The progressive increase of the 2790 cm^{-1} band with increasing oxalic, fumaric, or isophthalic

acid content directly evidences the formation of uncoordinated carboxyl groups, which subsequently serve as accessible binding sites for Eu^{3+} (Fig. 3). In fumarate-containing samples, the in-plane C=C stretching mode of the unsaturated linker appears near 790 cm^{-1}, in addition to the phenyl-ring vibrations of BDC. Raman spectra further support linker incorporation: the carboxylate C=O stretching modes at *ca.* 1410 cm^{-1} and 1610 cm^{-1} exhibit subtle shifts upon addition of the foreign ligands (Fig. S13, S15 and S17), consistent with modified coordination geometries of the carboxylate groups. Upon Eu^{3+} metalation, the O–H stretching band assigned to free carboxylic groups disappears entirely, confirming that Eu^{3+} is selectively coordinated by these defect-associated –COOH sites. Importantly, the Zr–O–C stretching band does not show noticeable shifting or splitting after Eu^{3+} incorporation, indicating that Eu^{3+} binds primarily at defect-related carboxylate positions without perturbing the Zr_6 cluster itself.

Fig. 4 shows the scanning electron microscopic (SEM) images and energy-dispersive X-ray spectroscopic (EDX) elemental mappings of UiO-66-0.25 ox-Eu, UiO-66-0.25 fum-Eu and UiO-66-0.1-ipa-Eu. No significant morphological changes are observed upon Eu^{3+} coordination compared with the respective pristine framework (Fig. S18 and S19). In all cases, the materials consist of granular aggregates of nearly monodisperse, sub-micrometer-sized particles, and the EDX maps confirm a homogeneous spatial distribution of Eu and Zr, indicating uniform metalation across the defective sites. These observations are consistent with previous SEM/EDX findings by Ragon *et al.*[49] and by Semivrazhskaya *et al.*,[52] who reported similarly narrow particle size distributions for UiO-66 synthesized under finely balanced metal-to-modulator ratios. Such conditions favor rapid nucleation relative to crystal growth, leading to the formation of ∼200 nm

crystallites. In the present system, a gradual increase in average crystallite size is observed with increasing oxalic, fumaric, or isophthalic acid content, suggesting a modulatory effect of the auxiliary ligands on the crystallization kinetics. This trend suggests that the defect-generating acids not only participate in the coordination but also modulate the apparent particle aggregation and likely also modulate the nucleation-growth balance, thereby influencing particle size and morphology.

Optical properties

Compared to their structural, catalytic, or adsorption characteristics, the optical properties of UiO-66-type materials have received considerably less attention. As a wide-bandgap insulator in the visible range, pristine UiO-66 cannot be considered an inorganic luminescent semiconductor.[53] According to the work of Mateo *et al.*, UiO-type frameworks exhibit remarkable long-term stability under irradiation in inert atmospheres, implying their potential for future applications in gas sensing and photocatalysis.[54] Diffuse reflectance UV-vis (DRUV-vis) spectra (Fig. S20) show the characteristic $\pi \rightarrow \pi^\star$ absorption bands of aromatic linkers. A slight narrowing of the absorption edge is observed upon incorporation of either aliphatic acids or isophthalic acid, indicating subtle modifications of the local electronic environment. The presence of foreign dicarboxylic acids is further evidenced by an increase in absorbance near 280 nm, attributable to transitions associated with the additional carboxylate species. (Besides incorporating isophthalic acid as a mixed linker, we also attempted to introduce 2,6-pyridinedicarboxylic acid was also attempted to generate additional pyridyl coordination sites.[55] However, our one-pot synthesis using this linker did not yield produce UiO-type phases.)

Weak absorption features attributable to Eu^{3+} are detected in all Eu-loaded samples (Fig. S20, inset). These correspond to Laporte-forbidden *f–f* transitions with inherently low molar absorption coefficients. Nonetheless, comparison of pristine and Eu-incorporated materials reveals clear additional absorptions, confirming successful incorporation of Eu^{3+} into the framework, consistent with structural and spectroscopic characterizations. Three-dimensional excitation–emission matrices (3D-EEM) of Eu-loaded samples with the lowest auxiliary-ligand contents are shown in Fig. 5. (full dataset in Fig. S21–S23). All materials exhibit the sharp-line emissions characteristic of Eu^{3+}. The spectral overlap between linker emission (∼400 nm) and Eu^{3+} absorption within the confined pore environment (short-range spatial proximity inside the pore cavities) suggest a Förster resonance energy transfer or Dexter energy transfer.[56,57] The corresponding two-dimensional excitation–emission spectra further allow clear assignment of the characteristic Eu^{3+} *f–f* transitions (Fig. S24–S26).

Optical O_2 gas sensing by dynamic quenching

The O_2-responsive luminescence of the Eu-loaded UiO-66 derivates was evaluated by monitoring the luminescence intensity change of the Eu^{3+} $^5D_0 \rightarrow {}^7F_2$ emission at 615 nm (excited at 300 nm) under alternating synthetic air (20.5 vol% O_2) and N_2 flows. The porous microenvironment and close donor–acceptor proximity between the aromatic linker (BDC or IPA) and Eu^{3+}
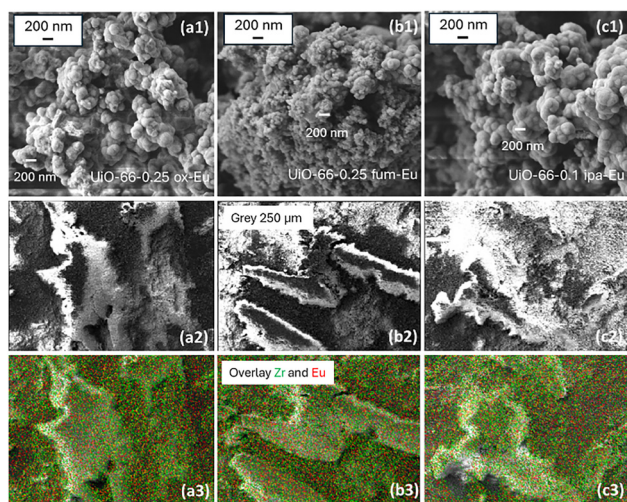

Fig. 4 (a) SEM micrographs of Eu-loaded UiO-66 derivatives with the lowest oxalic, fumaric and isophthalic acid concentrations. Samples synthesized with fumaric acid exhibit slightly smaller particle sizes compared to the oxalic acid- and isophthalic acid-containing materials. (b) and (c) EDX-elemental mapping confirms the spatial coexistence of Zr (framework Zr_6-clusters) and Eu (post-synthetic incorporation) within a representative 250 μm domain.
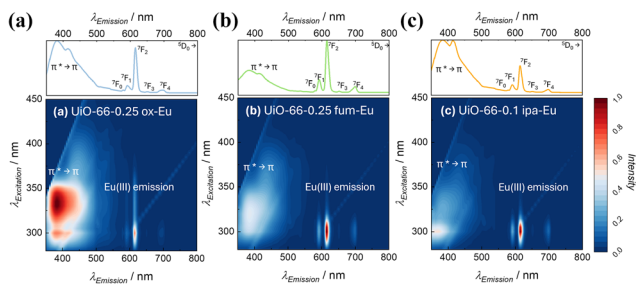
Fig. 5 Correlated three-dimensional excitation–emission spectra of europium-loaded UiO-66 derivatives with the lowest concentrations of auxiliary dicarboxylic acids: (a) UiO-66-0.25-ox-Eu, (b) UiO-66-0.25-fum-Eu and (c) UiO-66-0.1-ipa-Eu. All samples exhibit the characteristic sharp-line emissions of Eu^{3+}, together with linker-centered excitation bands, illustrating the coexistence of direct f–f excitation and linker-to-Eu^{3+} energy transfer pathways.

are critical for facilitating dynamic quenching. This is consistent with the complete absence of reversible O_2 response in UiO-66-0.75 ipa-Eu, which was previously shown to be amorphous and nonporous. For all porous Eu-functionalized UiO-66 samples, the luminescence is quenched rapidly upon O_2 introduction, with a response time of $t_{90,response}$ = 10 s, and fully recovers within $t_{90,recovery}$ = 10 s after switching back to N_2 purging (Fig. 6). This rapid and reversible behavior highlights
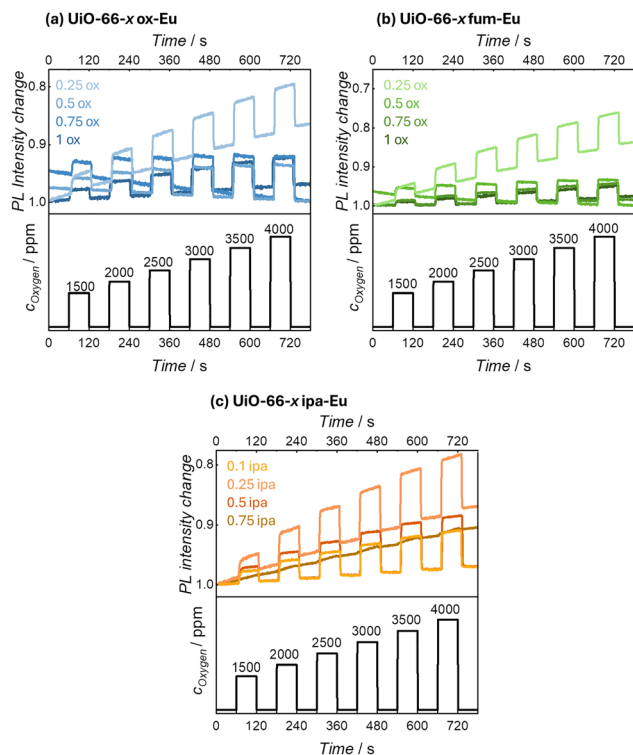

Fig. 6 Reversible O_2-sensing response of Eu-loaded UiO-66 derivatives over 780 s under alternating exposure to different O_2 concentrations. The luminescence intensity of Eu^{3+} $^5D_0 \rightarrow {}^7F_2$ emission at 614 nm was monitored as a function of time under 300 nm excitation while switching between O_2/N_2 mixtures. All porous Eu-UiO samples exhibit rapid and fully reversible luminescence quenching upon O_2 introduction, except UiO-66-0.75 ipa-Eu.

the dependence of quenching efficiency on (i) O_2-accessible microporosity, enabling fast gas diffusion into the local Eu^{3+} environment, and (ii) close-range donor–acceptor coupling, which allows triplet O_2 to efficiently deactivate the Eu-centered excited state via non-radiative pathways. This mechanism is consistent with related lanthanide-MOF O_2-sensing systems, such as the Tb^{3+}/BTC framework reported by Dou et al.,[6] in which spatially separated ligand-centered excited states act as energy donors that are effectively quenched by triplet O_2.

A Stern–Volmer analysis of the dependence of luminescence intensity on O_2 concentration (Fig. 7) reveals a pronounced deviation from linearity, marked by a concave curvature toward the x-axis. Such nonlinear behavior is characteristic for systems in which both dynamic (collisional) and static (pre-associated) quenching pathways contribute simultaneously.[58] (The reproducibility of the quenching response was validated using an independent sample batch, Fig. S27, confirming the robustness of the observed trends.) Time-resolved luminescence measurements further clarify the quenching mechanism. A significant shortening of the Eu^{3+} emission lifetime is observed when switching from N_2 to ambient air (ca. 20.5-vol% O_2), confirming that dynamic collisional quenching is the dominant deactivation process (Fig. 8). All samples show notable differences in lifetime between N_2 and air In case of UiO-66-0.75-ipa-Eu, the difference is very small, which is attributed to (i) its amorphous, nonporous nature, restricting O_2 penetration and (ii) the disordered coordination environment, lacking the confined sensitization pathway required for efficient O_2-induced quenching.
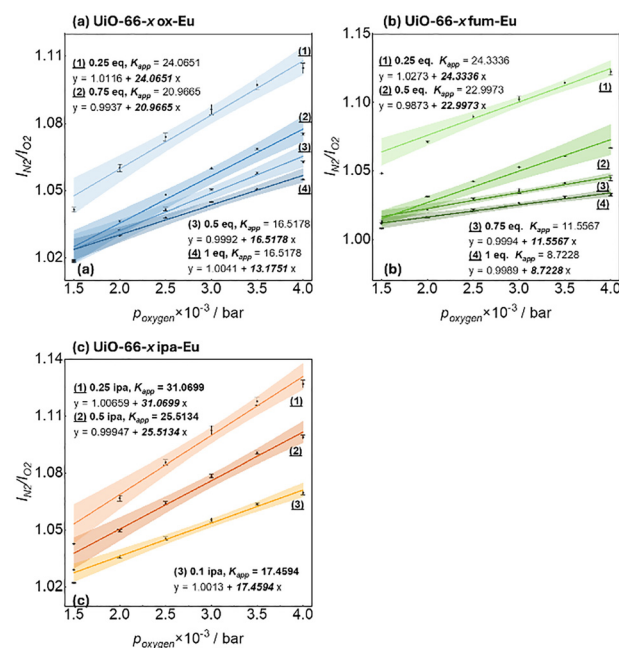

Fig. 7 Stern–Volmer plots of Eu-loaded (a) UiO-66-x-ox, (b) UiO-66-x-fum, and (c) UiO-66-x-ipa samples. The relative luminescence intensity I_0/I at 615 nm is plotted as a function of O_2 concentration. All samples exhibit nonlinear, concave-downward Stern–Volmer behaviour, indicative of combined dynamic and static quenching contributions. Shaded regions represent the 95% confidence intervals of the fitted lines.
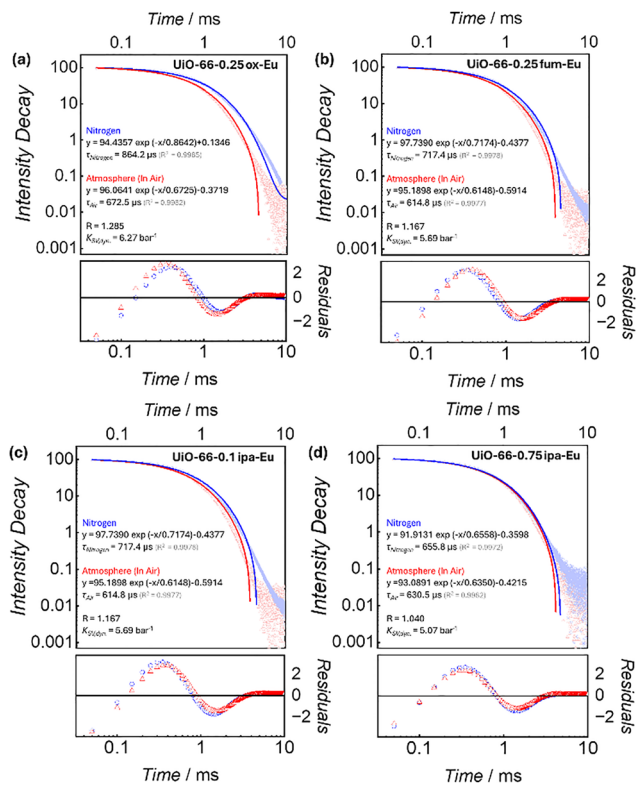
Fig. 8 Time-resolved photoluminescence decay of Eu-loaded UiO-66 derivatives measured under N_2 (blue) and ambient atmosphere (*ca.* 20.5 vol% O_2, red): (a) UiO-66-0.25-ox-Eu, (b) UiO-66-0.25-fum-Eu, (c) UiO-66-0.1-ipa-Eu and (d) UiO-66-0.75-ipa-Eu. A pronounced decrease in lifetime is observed upon exposure to O_2 for all porous samples, confirming dominant dynamic (collisional) quenching. In contrast, the amorphous/nonporous UiO-66-0.75-ipa-Eu shows minimal lifetime change, consistent with restricted oxygen accessibility. Residuals of the exponential fits are shown below each decay trace.

Collectively, these observations confirm that luminescence quenching in the Eu-UiO-66 systems is predominantly governed by collisional interactions between triplet O_2 and the Eu-centered (or linker-to-Eu sensitized) excited states.

To account for the coexistence of the two quenching pathways in porous materials, we propose an apparent Ster–Volmer constant $K_{SV,app}$ as shown in eqn (1),

$$K_{SV,app} = k_{q,app} \times \tau_0 \times H \qquad (1)$$

where $k_{q,app}$ is the apparent bimolecular quenching rate constant, τ_0 is the intrinsic luminophore lifetime in the absence of O_2, and H is the Henry constant describing O_2 adsorption in the framework pores. In diffusion-controlled regimes, $k_{q,app}$ scales with the effective O_2 diffusivity D_{eff} in the pore network, so that $K_{SV,app}$ reflects the combined effect of O_2 adsorption (*via* H) and transport (*via* D_{eff}).[59] In addition, from the lifetime ratio between N_2 and ambient air (20.5 vol% O_2), an effective dynamic Stern–Volmer constant can be calculated (see SI, Fig. S28–S30). The pronounced lifetime shortening unambiguously confirms the presence of dynamic collisional quenching. The fraction of the collisional Stern–Volmer contribution is significantly smaller than the overall apparent Stern–Volmer constant

$K_{SV,app}$, consistent with the marked concave-down deviation from linearity in the Stern–Volmer plots. This discrepancy indicates that, besides dynamic quenching, additional heterogeneous or "static-like" contributions are present. Such contributions most likely arise from the distribution of local Eu^{3+} environments and O_2-accessible sites within the defect-modulated pores. UiO-66-0.75-ipa-Eu shows local dynamic quenching without macroscopic sensing; it shows measurable dynamic lifetime quenching and no reversible intensity-based O_2 sensing. This indicates that only a small fraction of linker-Eu^{3+}, likely located near the particle surface, is dynamically quenched by adsorbed O_2, whereas the bulk of the amorphous, nonporous solid remains inaccessible to gas molecules. The limited O_2 transport (sensing) and N_2 transport (regeneration) prevents both quenching and recovery upon switching back to N_2, resulting in the absence of reversible sensing despite the presence of local dynamic quenching.

Fig. 9 shows the relationship between both the apparent Stern–Volmer constant $K_{app,SV}$ and the apparent bimolecular quenching constant $k_{q,app}$ and the specific BET surface area S_{BET}. For both constants, a maximum is observed for a medium-sized surface area (*ca.* 800 m² g⁻¹). This indicates that the O_2-quenching efficiency is maximized at an intermediate defect concentration. At lower defect densities, restricted pore apertures and limited free volume hinder O_2 transport, resulting in inefficient collisional quenching. As the defect concentration increases, O_2 accessibility (H) improves and diffusion pathways open, enhancing the quenching response. However, beyond a critical defect level, excessive ligand displacement disrupts the local packing, increases structural disorder, and weakens the donor–acceptor coupling between linker and Eu^{3+} sites. This reduces effective molecular diffusivity and diminishes the photophysical efficiency of the sensitization process. Therefore, the highest sensing performance emerges only when the framework simultaneously provides (i) sufficient microporosity for rapid O_2 ingress and (ii) a well-defined coordination environment that supports efficient energy transfer to Eu^{3+}. This defect
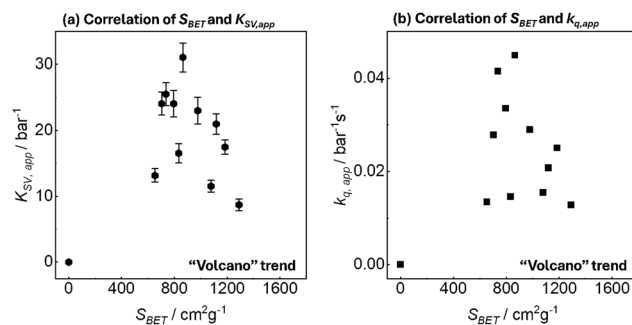

Fig. 9 Relationship between porosity and O_2-quenching efficiency in Eu-functionalized UiO-66 derivatives. (a) Apparent Stern–Volmer quenching constants K_{SV} plotted as a function of the specific BET surface area S_{BET}. (b) Corresponding apparent bimolecular quenching constants $k_{q,app} = K_{SV}/\tau_0$, showing the same non-monotonic dependence of S_{BET}, demonstrating that the trend arises from defect-modulated O_2 accessibility and transport (*via* Henry constant H and diffusion constant D_{eff}) rather than changes in the intrinsic Eu^{3+} photophysical properties.

structure-performance relationship highlights the importance of balancing porosity generation with preservation of photophysical active coordination sites (Fig. 9).

Conclusions

In summary, this work establishes a quantitative structure–property relationship linking defect-modulated porosity in UiO-66 to the O_2-quenching response of Eu^{3+}-functionalized frameworks. By systematically introducing three distinct defect types, we observe that vacancy formation enhances the accessibility of Eu^{3+} sites and facilitates O_2 diffusion, thereby strengthening the dynamic quenching pathway while simultaneously introducing a measurable static contribution. Time-resolved luminescence measurements confirm a pronounced lifetime shortening under O_2, evidencing the collisional nature of the deactivation process. The nonlinear Stern–Volmer behaviour observed across all defect-engineered samples is captured by an apparent quenching constant $K_{app,SV}$, which incorporates intrinsic photophysical parameters and a defect-dependent structural factor reflecting oxygen adsorption and transport. Importantly, the volcano-type dependence of O_2 sensitivity on defect concentration reveals that optimal sensing performance arises only when Eu^{3+} exposure and micropore transport are simultaneously balanced. Overall, this study provides a mechanistic framework for defect-governed triplet quenching in porous solids and offers general design principles for tuning porosity, coordination environments, and gas-transport properties in lanthanide-based optical oxygen sensors.

Author contributions

Z. Z.: conceptualization, methodology, investigation, visualization, writing – original draft. M. T.: supervision, writing – review & editing, data curation, project administration.

Conflicts of interest

There are no conflicts to declare.

Data availability

All data supporting the findings of this study are available within the article and its supplementary information (SI). Supplementary information includes experimental details, additional characterization data, and supplementary figures and tables. See DOI: https://doi.org/10.1039/d5tc04319k.

Notes and references

1   X. Wang and O. S. Wolfbeis, *Chem. Soc. Rev.*, 2014, **43**, 3666–3761.
2   R. Ramamoorthy, P. K. Dutta and S. A. Akbar, *Chem. Sens.*, 2003, **38**, 4271–4282.
3   M. D. Allendorf, C. A. Bauer, R. K. Bhakta and R. J. T. Houk, *Chem. Soc. Rev.*, 2009, **38**, 1330.
4   J.-X. Wang, J. Yin, O. Shekhah, O. M. Bakr, M. Eddaoudi and O. F. Mohammed, *ACS Appl. Mater. Interfaces*, 2022, **14**, 9970–9986.
5   J. An, C. M. Shade, D. A. Chengelis-Czegan, S. Petoud and N. L. Rosi, *J. Am. Chem. Soc.*, 2011, **133**, 1220–1223.
6   Z. Dou, J. Yu, Y. Cui, Y. Yang, Z. Wang, D. Yang and G. Qian, *J. Am. Chem. Soc.*, 2014, **136**, 5527–5530.
7   X. Qiao, Z. Ma, L. Si, W. Ding and G. Xu, *Sens. Actuators, B*, 2019, **299**, 126978.
8   J.-W. Ye, H.-L. Zhou, S.-Y. Liu, X.-N. Cheng, R.-B. Lin, X.-L. Qi, J.-P. Zhang and X.-M. Chen, *Chem. Mater.*, 2015, **27**, 8255–8260.
9   T. Burger, M. D. J. Velásquez-Hernández, R. Saf, S. M. Borisov and C. Slugovc, *J. Mater. Chem. C*, 2022, **10**, 13262–13267.
10 X.-Y. Dong, Y. Si, J.-S. Yang, C. Zhang, Z. Han, P. Luo, Z.-Y. Wang, S.-Q. Zang and T. C. W. Mak, *Nat. Commun.*, 2020, **11**, 3678.
11 S. Liu, X. Qi, R. Lin, X. Cheng, P. Liao, J. Zhang and X. Chen, *Adv. Funct. Mater.*, 2014, **24**, 5866–5872.
12 Z. Zhao, C. Weinberger, J. Steube, M. Bauer, M. Brehm and M. Tiemann, *Adv. Funct. Mater.*, 2025, e11190.
13 H. Furukawa, F. Gándara, Y.-B. Zhang, J. Jiang, W. L. Queen, M. R. Hudson and O. M. Yaghi, *J. Am. Chem. Soc.*, 2014, **136**, 4369–4381.
14 S. Wang, N. Xhaferaj, M. Wahiduzzaman, K. Oyekan, X. Li, K. Wei, B. Zheng, A. Tissot, J. Marrot, W. Shepard, C. Martineau-Corcos, Y. Filinchuk, K. Tan, G. Maurin and C. Serre, *J. Am. Chem. Soc.*, 2019, **141**, 17207–17216.
15 S. Wang, M. Wahiduzzaman, L. Davis, A. Tissot, W. Shepard, J. Marrot, C. Martineau-Corcos, D. Hamdane, G. Maurin, S. Devautour-Vinot and C. Serre, *Nat. Commun.*, 2018, **9**, 4937.
16 J. H. Cavka, S. Jakobsen, U. Olsbye, N. Guillou, C. Lamberti, S. Bordiga and K. P. Lillerud, *J. Am. Chem. Soc.*, 2008, **130**, 13850–13851.
17 C. S. Cox, E. Slavich, L. K. Macreadie, L. K. McKemmish and M. Lessio, *Chem. Mater.*, 2023, **35**, 3057–3072.
18 G. C. Shearer, S. Chavan, J. Ethiraj, J. G. Vitillo, S. Svelle, U. Olsbye, C. Lamberti, S. Bordiga and K. P. Lillerud, *Chem. Mater.*, 2014, **26**, 4068–4071.
19 J. B. DeCoste, T. J. Demasky, M. J. Katz, O. K. Farha and J. T. Hupp, *New J. Chem.*, 2015, **39**, 2396–2399.
20 R. Oozeerally, D. L. Burnett, T. W. Chamberlain, R. J. Kashtiban, S. Huband, R. I. Walton and V. Degirmenci, *ChemCatChem*, 2021, **13**, 2517–2529.
21 J. Y. Song, I. Ahmed, P. W. Seo and S. H. Jhung, *ACS Appl. Mater. Interfaces*, 2016, **8**, 27394–27402.
22 T. Kasper, M. Pavan and K. Müller-Buschbaum, *J. Mater. Chem. A*, 2024, **12**, 769–780.
23 T. Kasper, J. Burkhart and K. Müller-Buschbaum, *ChemPhotoChem*, 2024, **8**, e202300329.
24 M. J. Katz, Z. J. Brown, Y. J. Colón, P. W. Siu, K. A. Scheidt, R. Q. Snurr, J. T. Hupp and O. K. Farha, *Chem. Commun.*, 2013, **49**, 9449.

25 H. Woo, A. M. Devlin and A. J. Matzger, *J. Am. Chem. Soc.*, 2023, **145**, 18634–18641.

26 J. Ma, A. P. Kalenak, A. G. Wong-Foy and A. J. Matzger, *Angew. Chem., Int. Ed.*, 2017, **56**, 14810–14813.

27 C. Caratelli, J. Hajek, E. J. Meijer, M. Waroquier and V. Van Speybroeck, *Chem. – Eur. J.*, 2019, **25**, 15315–15325.

28 C. Caratelli, J. Hajek, S. M. J. Rogge, S. Vandenbrande, E. J. Meijer, M. Waroquier and V. Van Speybroeck, *Chem-PhysChem*, 2018, **19**, 420–429.

29 K. Momma and F. Izumi, *J. Appl. Crystallogr.*, 2011, **44**, 1272–1276.

30 J. Rouquerol, P. Llewellyn and F. Rouquerol, *Stud. Surf. Sci. Catal.*, 2007, 49–56.

31 M. Rubin, *Sol. Energy Mater.*, 1985, **12**, 275–288.

32 S. Tatay, S. Martínez-Giménez, A. Rubio-Gaspar, E. Gómez-Oliveira, J. Castells-Gil, Z. Dong, Á. Mayoral, N. Almora-Barrios, N. M. Padial and C. Martí-Gastaldo, *Nat. Commun.*, 2023, **14**, 6962.

33 Y. Feng, Q. Chen, M. Jiang and J. Yao, *Ind. Eng. Chem. Res.*, 2019, **58**, 17646–17659.

34 G. C. Shearer, S. Chavan, S. Bordiga, S. Svelle, U. Olsbye and K. P. Lillerud, *Chem. Mater.*, 2016, **28**, 3749–3761.

35 I. Abánades Lázaro, S. Haddad, J. M. Rodrigo-Muñoz, C. Orellana-Tavra, V. Del Pozo, D. Fairen-Jimenez and R. S. Forgan, *ACS Appl. Mater. Interfaces*, 2018, **10**, 5255–5268.

36 O. V. Gutov, S. Molina, E. C. Escudero-Adán and A. Shafir, *Chem. – Eur. J.*, 2016, **22**, 13582–13587.

37 A. Alemayehu, A. Zakharanka and V. Tyrpekl, *ACS Omega*, 2022, **7**, 12288–12295.

38 X.-F. Tan, J. Zhou, L. Fu, H.-P. Xiao, H.-H. Zou and Q. Tang, *Dalton Trans.*, 2016, **45**, 5253–5261.

39 L.-X. You, B.-B. Zhao, H.-J. Liu, S.-J. Wang, G. Xiong, Y.-K. He, F. Ding, J. J. Joos, P. F. Smet and Y.-G. Sun, *CrystEngComm*, 2018, **20**, 615–623.

40 S. J. D. Smith, K. Konstas, C. H. Lau, Y. M. Gozukara, C. D. Easton, R. J. Mulder, B. P. Ladewig and M. R. Hill, *Cryst. Growth Des.*, 2017, **17**, 4384–4392.

41 D.-X. Xue, Y. Belmabkhout, O. Shekhah, H. Jiang, K. Adil, A. J. Cairns and M. Eddaoudi, *J. Am. Chem. Soc.*, 2015, **137**, 5034–5040.

42 W. Liang, C. J. Coghlan, F. Ragon, M. Rubio-Martinez, D. M. D'Alessandro and R. Babarao, *Dalton Trans.*, 2016, **45**, 4496–4500.

43 C. W. Abney, K. M. L. Taylor-Pashow, S. R. Russell, Y. Chen, R. Samantaray, J. V. Lockard and W. Lin, *Chem. Mater.*, 2014, **26**, 5231–5243.

44 D. Bůžek, S. Adamec, K. Lang and J. Demel, *Inorg. Chem. Front.*, 2021, **8**, 720–734.

45 G. Zahn, P. Zerner, J. Lippke, F. L. Kempf, S. Lilienthal, C. A. Schröder, A. M. Schneider and P. Behrens, *CrystEng-Comm*, 2014, **16**, 9198–9207.

46 M. Taddei, R. J. Wakeham, A. Koutsianos, E. Andreoli and A. R. Barron, *Angew. Chem., Int. Ed.*, 2018, **57**, 3349–3359.

47 M. Kim, J. F. Cahill, Y. Su, K. A. Prather and S. M. Cohen, *Dalton Trans.*, 2012, **41**, 18082–18088.

48 Y. Lee, S. Kim, H. Fei, J. K. Kang and S. M. Cohen, *Chem. Commun.*, 2015, **51**, 16549–16552.

49 F. Ragon, P. Horcajada, H. Chevreau, Y. K. Hwang, U.-H. Lee, S. R. Miller, T. Devic, J.-S. Chang and C. Serre, *Inorg. Chem.*, 2014, **53**, 2491–2500.

50 K. I. Hadjiivanov, D. A. Panayotov, M. Y. Mihaylov, E. Z. Ivanova, K. K. Chakarova, S. M. Andonova and N. L. Drenchev, *Chem. Rev.*, 2021, **121**, 1286–1424.

51 L. Valenzano, B. Civalleri, S. Chavan, S. Bordiga, M. H. Nilsen, S. Jakobsen, K. P. Lillerud and C. Lamberti, *Chem. Mater.*, 2011, **23**, 1700–1718.

52 O. O. Semivrazhskaya, D. Salionov, A. H. Clark, N. P. M. Casati, M. Nachtegaal, M. Ranocchiari, S. Bjelić, R. Verel, J. A. Van Bokhoven and V. L. Sushkevich, *Small*, 2023, **19**, 2305771.

53 K. Hendrickx, J. J. Joos, A. De Vos, D. Poelman, P. F. Smet, V. Van Speybroeck, P. Van Der Voort and K. Lejaeghere, *Inorg. Chem.*, 2018, **57**, 5463–5474.

54 D. Mateo, A. Santiago-Portillo, J. Albero, S. Navalón, M. Alvaro and H. García, *Angew. Chem., Int. Ed.*, 2019, **58**, 18007–18012.

55 Y.-N. Zeng, H.-Q. Zheng, X.-H. He, G.-J. Cao, B. Wang, K. Wu and Z.-J. Lin, *Dalton Trans.*, 2020, **49**, 9680–9687.

56 J. Brennan, Z. M. Soilis, V. P. Cohen, R. R. Frontiera and N. L. Rosi, *J. Phys. Chem. C*, 2025, **129**, 20471–20479.

57 P. A. Tanner, L. Zhou, C. Duan and K.-L. Wong, *Chem. Soc. Rev.*, 2018, **47**, 5234–5265.

58 L. K. Fraiji, D. M. Hayes and T. C. Werner, *J. Chem. Educ.*, 1992, **69**, 424.

59 I. Dalfen and S. M. Borisov, *Anal. Bioanal. Chem.*, 2022, **414**, 4311–4330.